Accurate X-Ray Absorption Predictions for Transition Metal Oxides: An Advanced Self-Consistent-Field Approach Inspired by Many-Body Perturbation Theory

Yufeng Liang,[1] John Vinson,[2] Sri Pemmeraju,[1] Walter Drisdell,[3] Eric L. Shirley,[2] and David Prendergast[1]

[1] *The Molecular Foundry, Lawrence Berkeley National Laboratory, Berkeley, CA 94720, USA*
[2] *National Institute of Standards and Technology (NIST), Gaithersburg, MD 20899, USA*
[3] *Chemical Science Division, Lawrence Berkeley National Laboratory, Berkeley, CA 94720, USA*

I. STRUCTURES

The structures used for first-principles core-level calculations are taken from the Crystallography Open Database (COD) at http://www.crystallography.net with COD IDs listed in Table I, together with the supercell size for modeling X-ray excitations in the full core-hole (FCH) approach.

II. ΔSCF CORE-HOLE APPROACH

The FCH calculations are performed using the ShirleyXAS code at the Molecular Foundry, which couples to the Quantum Espresso source code package [1]. We employ the Vanderbilt ultrasoft pseudopentials with a semicore electron configuration $3s^2 3p^6 4s^2 3d^n$ for the transition metal atoms. X-ray excitations at the O K edge are modeled within the core-hole impurity model, by replacing the pseudopotential of one O atom in a supercell of ~ 1 nm in each dimension with its core-excited version (using a $1s^1$ core configuration). To produce numerically converged XAS spectra, we use the Shirley interpolation scheme[2] to efficiently sample the Brillouin zone of the supercell with a $5 \times 5 \times 5$ k-point grid. The final spectra are convoluted with a Gaussian broadening of 0.5 eV and aligned with the near-edge region in experiment. For the rutile group, we find that excellent convergence of XAS has been achieved with a $2 \times 2 \times 3$ supercell for TiO_2. Increasing the cell size to a dimension of $3 \times 3 \times 4$ does not lead to discernible changes, as is shown in Fig. 1 (a). Good convergence has also been achieved with respect to the plane-wave energy cutoff (30 Ryd $\rightarrow$ 40 Ryd) of the wavefunctions (Fig. 1 (b)). A change from the Perdew-Burke-Ernzerhof (PBE) exchange-correlation functional within the generalized-gradient approximation (GGA) to the Perdew-Zunger (PZ) functional within the local density approximation (LDA) slightly redshifts the extended absorption feature above 535 eV, but it does not affect the near-edge feature. For the d^0 TiO_2, we also experiment on the choice of core-hole approach, FCH and XCH. The latter includes one core-excited electron at the bottom of the unoccupied manifold. Again, this does not alter the near-edge feature.

The failure of FCH to produce correct pre-edge intensity could be due to the empirical Hubbard U parameter that can strongly affect the TM-d-O-$2p$ hybridization. Furthermore, there is no guarantee that the U values extracted from ground-state calculations can be transferred to a core-excited system. We test the changes of the pre-edge lineshape for VO_2 and CrO_2 with respect to a wide range of U. As displayed in Fig. 2 (b), none of the chosen U values corrects the intensity of the t_{2g} peak; vanishing U have almost no impact on the lineshape, whereas large U further split the second feature ($\sim$ 532 eV) into two peaks. These numerical tests highlight that there are fundamental shortcoming within the FCH approach the prevent it from correctly reproducing O K edge fingerprints of TMOs.

Further insight into the failure of the ΔSCF method in predicting O K edges of TMOs can be gained from the projected density-of-states (PDOS) of the core-excited impurity configuration. Fig. 3 displays the PDOS of three distinct types of oxygen atoms in the $2 \times 2 \times 3$ supercell of VO_2: the single core-excited atom (dark red), its nearest neighbor (red), and the farthest atom from the excited one (orange). Since good convergence has been achieved in this supercell size, the most distant O can be considered as unaffected by the core hole. The core-hole attractive effects are evident from the PDOS of the excited O, which displays three sharp localized peaks near -9 eV below the fermi level, E_f. This is a

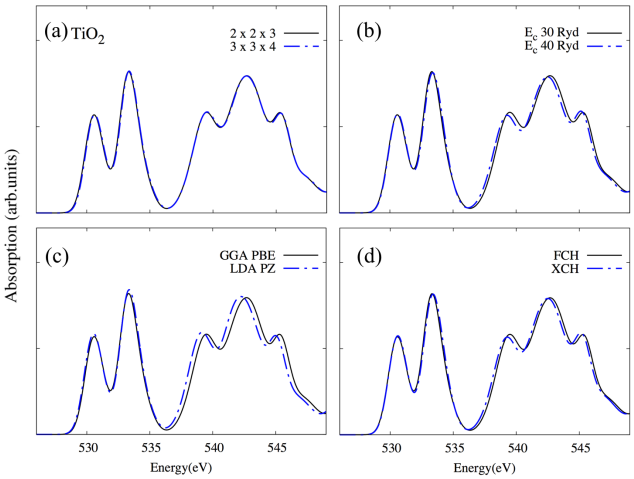

FIG. 1. Numerical tests of the validity of the core-hole approach in predicting XAS of TiO_2. The figures show the FCH-XAS with the $2 \times 2 \times 3$ and $3 \times 3 \times 4$ supercells (a) and with plane-wave energy cutoff E_c of 30 and 40 Ryd (b), a comparison of GGA-PBE versus LDA-PZ functionals (c) and FCH versus XCH (d).

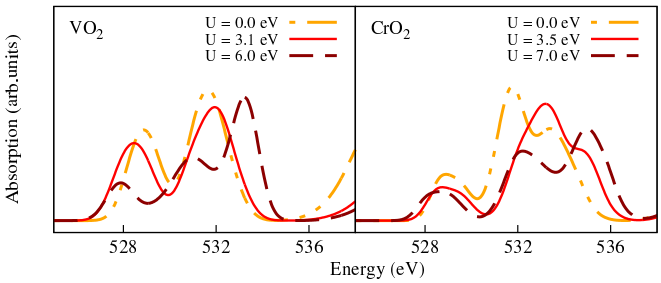

FIG. 2. Comparison of FCH spectra with a wide range of U value employed in the DFT+U theory

clear sign of significant charge transfer onto the p_x, p_y, and p_z orbitals of the core-excited atom in response to the attractive core-hole potential. Accompanying this charge transfer is a substantial decrease in the unoccupied PDOS distribution ($0 \sim 4$ eV) in the vicinity of the excited site, as compared with the unexcited atom (orange) [greater detail is provided in a narrower energy range in Fig. 3 (b)]. The integrated ($0 \sim 2$ eV) unoccupied PDOS shrinks to less than 50% of the distant O atom in the presence of the on-site core hole. *This is the primary reason for why the near-edge feature appears weak in the one-body core-hole approach.* Even more dramatic DOS migration from the empty to the occupied manifold is observed from the spin-resolved PDOS of the metallic CrO_2 in Fig. 3 (c) and (d). The states near E_f are mainly defined by the t_{2g} orbitals of majority spin (the red and orange curve), which forms a distinct peak in PDOS through hybridization with O 2p character. This peak almost disappears after the static core hole is introduced. Similar to VO_2, its spectral weight is largely transferred to the states below E_f. The peaks at higher energies (~ 4 eV in Fig 3 (d)) above E_f, however, suffer less from the reduction in intensity resulting from the core-hole potential. From our observations we can deduce that: the more metallic the oxides is, the more the peak intensity will be underestimated.

The core-hole effects in FCH also play a role in the redshift of the PDOS. This is clearly evident in the e_g features because these orbitals are pointing towards the excited O atom and are more susceptible to core-hole attraction compared to the t_{2g} orbitals. As shown in Fig. 3 (b) and (d), the core-hole effects redshift the e_g features by ~ 1 eV in both VO_2 and CrO_2. Furthermore, it is worth noting that FCH does not create localized mid-gap states in TMOs. The O core hole serves to lower the O $2p$ levels and hence reduce the TM-$3d$-O-$2p$ hybridization. This is also why near-edge the sharp excitonic sharp peaks are not reproduced by the core-hole approach.

III. BETHE-SALPETER EQUATION CALCULATIONS

In BSE calculations, we employ the semilocal GGA-PBE pseudopotentials as generated by the OPIUM code. These pseudopotentials have a semicore configuration $3p^6 4s^2 3d^n$. The ground-state calculations and wavefunction generation are performed using Quantum Espresso. For generating O K edge in TMOs, we use the DFT+U orbitals (ψ_c and ε_c) as input for the BSE calculation. A large energy cutoff of 160 Ryd is used for the plane-wave basis set of ψ_c. To converge the dielectric function, 10 times as many conduction bands as valence bands are included in the RPA calculation for W. The spectra are obtained on a $6 \times 6 \times 6$ k-point grid for all TMOs and numerically convoluted with a Lorentzian broadening of 0.5 eV.

For the metallic CrO_2,the BSE spectrum converges at an energy cutoff, E_c, of 80 Ry. The spectra calculated with $E_c = 120$ Ry or 160 Ry are practically identical. Furthermore, the BSE spectrum also converges on a $6 \times 6 \times 6$ k-grid; using a $10 \times 10 \times 10$ k-grid does not lead to significant changes across the computed spectral energy range.

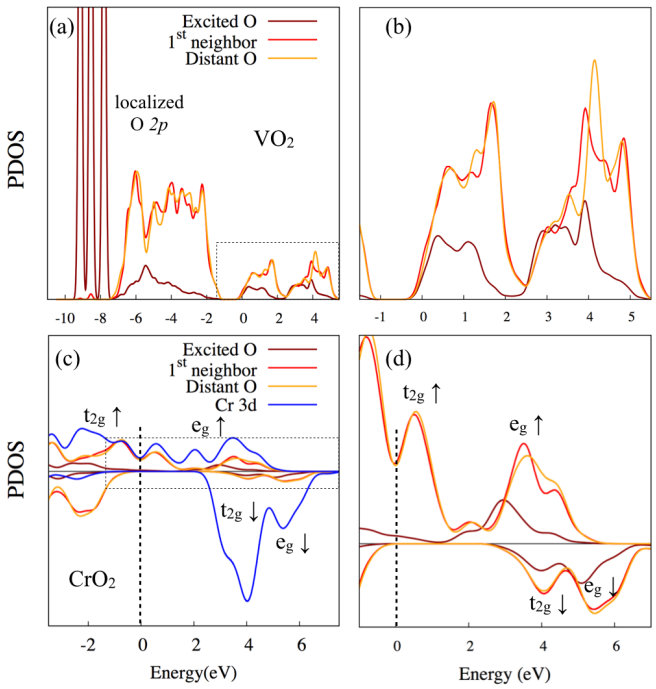

FIG. 3. Projected density-of-states (PDOS) of the rutile VO_2 ((a) and (b)) and CrO_2 ((c) and (d)). The fermi level is pinned at 0 eV, as marked by the vertical dashed lines. The three spikes near -9 eV are the localized O $2p$ orbitals. The right panels are enlarged view of the dashed frames on the left panels.

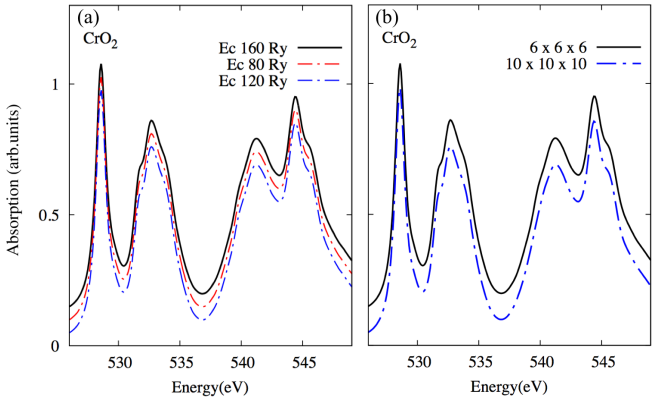

FIG. 4. Convergence test of O K-edge of CrO_2 with respect to energy cutoff Ec (a) and BSE k-grid density (b). Spectra are slightly offset for comparison.

IV. MANY-BODY ΔSCF CORE-HOLE APPROACH

We first show how to derive the determinant form the of the amplitude A_c^f from $\langle\Psi_f|\boldsymbol{\epsilon}\cdot\boldsymbol{R}|\Psi_i\rangle$ based on the independent-KS-orbital approximation. Since the dipole operator is one-body, it can be expanded with single-particle orbitals

$$\boldsymbol{\epsilon}\cdot\boldsymbol{R} = \sum_i a_i^\dagger h^\dagger \langle\psi_i|\boldsymbol{\epsilon}\cdot\boldsymbol{r}|\psi_h\rangle + c.c. \tag{1}$$

where $a_i^\dagger$ and $h^\dagger$ are (i^{th}) valence electron and core-hole creation operators, respectively, and ψ_i are ψ_h are the corresponding single-particle orbitals from the initial state. i iterates over all the valence orbitals – both occupied and unoccupied. Projection onto valence-to-valence transitions is omitted here because they are not relevant for core-hole excitations. When $a_i^\dagger h^\dagger$ acts on the ground state $|\Psi_i\rangle$ with N valence electrons the core level of interest, it produces a state with one less core electron and $N+1$ valence electrons. Therefore index i must correspond to an unoccupied orbital in order not to annihilate the resulting state, and we relabel it as c. Hence, $a_c^\dagger h^\dagger|\Psi_i\rangle$ gives rise to a many-body state with the N lowest-energy valence orbitals and the c^{th} orbital ($c > N$) occupied, which we denote as $|\Psi_i^c\rangle \equiv a_c^\dagger h|\Psi_i\rangle$. Within the independent-KS-orbital approximation, $|\Psi_i^c\rangle$ can be expressed in terms of a *single* Slater determinant.

Now we adopt a compact notation using the second quantization formalism rather than representing the many-body state in a determinant form.

$$|\Psi_i^c\rangle = a_c^\dagger \prod_{n=1}^{N} a_n^\dagger |0\rangle \tag{2}$$

where $|0\rangle$ is the null state in which there are no electrons. Similarly, for the final state $|\Psi_f\rangle$, defined by the final-state orbital configuration $f = (f_1, f_2, \ldots, f_N, f_{N+1})$, we have

$$|\Psi_f\rangle = \prod_{n=1}^{N+1} \tilde{a}_{f_n}^\dagger |0\rangle \tag{3}$$

Here, $\tilde{a}_i$ is the electron creation operator in the i^{th} final-state orbital. With these forms of many-body wavefunctions, the transition amplitude can be re-expressed as

$$\langle\Psi_f|\boldsymbol{\epsilon}\cdot\boldsymbol{R}|\Psi_i\rangle = \sum_c^{\text{empty}} \langle\Psi_f|\Psi_i^c\rangle\langle\psi_c|\boldsymbol{\epsilon}\cdot\boldsymbol{r}|\psi_h\rangle \tag{4}$$

We define a linear transformation to represent the creation operators of the final state orbitals in terms of those of the initial state:

$$\tilde{a_i}^\dagger = \sum_{j=1}^{M} \xi_{ij} a_j^\dagger \tag{5}$$

where M is size of the orbital space (In principle M defines a truncation of the infinite one-body Hilbert space.). With this transformation, the many-body final state can be obtained entirely within the initial-state representation.

$$\begin{aligned} |\Psi_f\rangle &= \prod_{n=1}^{N+1} \tilde{a}_{f_n}^\dagger |0\rangle \\ &= \left(\sum_{j_1=1}^{M} \xi_{f_1 j_1} a_{j_1}^\dagger\right) \cdots \left(\sum_{j_{N+1}=1}^{M} \xi_{f_{N+1} j_{N+1}} a_{j_{N+1}}^\dagger\right) |0\rangle \\ &= \sum_{j_1, j_2, \cdots, j_{N+1}=1}^{M} \xi_{f_1 j_1} \cdots \xi_{f_{N+1} j_{N+1}} \left(\prod_{n=1}^{N+1} a_{j_n}^\dagger\right) |0\rangle \end{aligned} \tag{6}$$

where there are M^{N+1} terms in the final summation above, one for each permutation $j = (j_1, \cdots, j_{N+1})$ defined by choosing $N+1$ electrons from the set of M initial-state orbitals.

Each of of these terms $\prod_{n=1}^{N+1} a_{j_n}^\dagger$ makes non-zero contribution to $\langle\Psi^f|\Psi_i^c\rangle$ only when the $N+1$ indices in $j = (j_1, \cdots, j_{N+1})$ is permutation of $(1, \cdots, N, c)$. There are $(N+1)!$ such permutations and the many-body overlap (conjugate) can be reduced to

$$\langle\Psi^f|\Psi_i^c\rangle^* = \sum_{j=(j_1,\ldots,j_{N+1})} \varepsilon_j \xi_{f_1 j_1} \cdots \xi_{f_{N+1} j_{N+1}} \tag{7}$$

where the Levi-Civita symbol ε_j reflects whether the indices $j = (j_1, \cdots, j_{N+1})$ is an even ($\varepsilon_j = 1$) or odd ($\varepsilon_j = -1$) permutation of $(1, \cdots, N, c)$. This sign change results from reordering the fermionic operators. Now it is clear that the many-body overlap defines a determinant of a subset of the orbital transformation coefficients. If we imagine the entire set of ξ_{ij} as an $M \times M$ matrix, then the determinant is that of a submatrix defined by the overlap of a specific selection of $N+1$ rows and columns:

the rows defined by the particular final state orbital configuration f and the columns chosen from the accessible initial state orbital indices, defined uniquely by c for excitations from the ground state:

$$\langle \Psi_f | \Psi_i^c \rangle^* = A_c^f = \det \begin{bmatrix} \xi_{f_1,1} & \xi_{f_1,2} & \cdots & \xi_{f_1,N} & \xi_{f_1,c} \\ \xi_{f_2,1} & \xi_{f_2,2} & \cdots & \xi_{f_2,N} & \xi_{f_2,c} \\ \vdots & & \ddots & & \vdots \\ \xi_{f_{N+1},1} & \xi_{f_{N+1},2} & \cdots & \xi_{f_{N+1},N} & \xi_{f_{N+1},c} \end{bmatrix} \quad (8)$$

In practice, the transition amplitude can be built from the two SCF calculations which define the initial state and final state orbital spaces. $\langle \psi_c | \boldsymbol{\epsilon} \cdot \boldsymbol{r} | \psi_h \rangle$ can be readily obtained from the initial state alone. The coefficients ξ_{ij} used in the determinant expression for the amplitude A_c^f, and defined with respect to construction operators in Eq. 5 are evaluated as $\xi_{ij} = \langle \tilde{\psi}_i | \psi_j \rangle$. They form a transformation matrix from the initial-state orbital basis $|\psi_j\rangle$ to the final-state orbital basis $|\tilde{\psi}_i\rangle$. The utilized spectrum of Kohn-Sham orbitals in both the initial-state and final-state pictures are obtained based on the converged charge density of the corresponding supercell configuration. At present, only the wavefunctions at the Γ-point are employed for producing the spectra. For reference, the TiO_2 and CrO_2 supercells contain 576 and 624 electrons respectively and we calculate the transformation matrix $(\xi_{ij})_{M\times M}$ up to $M = 600$ and 1122 orbitals for the two cases. The number of states used in CrO_2 is almost double that used in TiO_2 because of the lifted spin degeneracy.

To explore the spectrum of non-interacting many-electron final states efficiently and without repitition, the indices $f = (f_1, f_2, \cdots, f_{N+1})$ are generated using a depth-first search algorithm. We start from the the single *e*-*h*-pair configurations $f^{(1)} = (1, 2, \cdots, N, f_{N+1})$, beginning from $f_{N+1} = N + 1$. At each recursion, we replace index i, chosen from one of the first N indices in a $f^{(n-1)}$ configuration with index $j > N$ to produce a higher-order $f^{(n)}$ configuration to incorporate the additional $i \to j$ *e*-*h*-pair. In the next recursion, we start from the next lower index than the replaced index and replace it with the next higher unoccupied index with respect to last recursion, so as to avoid double counting, since the order of orbitals does not matter for the definition of a configuration. Certainly, this will lead to an exponentially large number of states but fortunately good convergence has been achieved at the $f^{(2)}$ level for TiO_2 and CrO_2.

The single-body matrix element $w_c = \langle \psi_c | \boldsymbol{\epsilon} \cdot \boldsymbol{r} | \psi_h \rangle$ is obtained from projecting each initial-state orbital onto the atomic orbitals that lead to bright transitions, i.e., the O $2p$ manifold in this case.

[1] Paolo Giannozzi, Stefano Baroni, Nicola Bonini, Matteo Calandra, Roberto Car, Carlo Cavazzoni, Davide Ceresoli, Guido L Chiarotti, Matteo Cococcioni, Ismaila Dabo, Andrea Dal Corso, Stefano de Gironcoli, Stefano Fabris, Guido Fratesi, Ralph Gebauer, Uwe Gerstmann, Christos Gougoussis, Anton Kokalj, Michele Lazzeri, Layla Martin-Samos, Nicola Marzari, Francesco Mauri, Riccardo Mazzarello, Stefano Paolini, Alfredo Pasquarello, Lorenzo Paulatto, Carlo Sbraccia, Sandro Scandolo, Gabriele Sclauzero, Ari P Seitsonen, Alexander Smogunov, Paolo Umari, and Renata M Wentzcovitch. Quantum espresso: a modular and open-source software project for quantum simulations of materials. *Journal of Physics: Condensed Matter*, 21(39):395502 (19pp), 2009.

[2] Eric L Shirley. Optimal basis sets for detailed brillouin-zone integrations. *Physical Review B*, 54(23):16464, 1996.

TABLE I.

	COD ID	supercell dimension	supercell size (nm^3)
TiO_2	4102355	$2 \times 2 \times 3$	$0.9178 \times 0.9178 \times 0.8873$
VO_2	4336391	$2 \times 2 \times 3$	$0.9197 \times 0.9197 \times 0.8554$
CrO_2	9007540	$2 \times 2 \times 3$	$0.8842 \times 0.8842 \times 0.8751$
α-Fe_2O_3	9000139	$2 \times 2 \times 2$	$1.0869 \times 1.0869 \times 1.0869$
$SrTiO_3$	1512124	$3 \times 3 \times 3$	$1.1697 \times 1.1697 \times 1.1697$